Coherence properties of the European XFEL

2010 New J. Phys. 12 035021

(http://iopscience.iop.org/1367-2630/12/3/035021)

New Journal of Physics
The open-access journal for physics

Coherence properties of the European XFEL

G Geloni[1], E Saldin[2], L Samoylova[1], E Schneidmiller[2], H Sinn[1], Th Tschentscher[1,3] and M Yurkov[2]

[1] European XFEL, Albert-Einstein-Ring 19, 22761 Hamburg, Germany
[2] Deutsches Elektronen-Synchrotron DESY, 22607 Hamburg, Germany
E-mail: thomas.tschentscher@xfel.eu

New Journal of Physics **12** (2010) 035021 (15pp)
Received 1 December 2009
Published 31 March 2010
Online at http://www.njp.org/
doi:10.1088/1367-2630/12/3/035021

Abstract. The European x-ray free-electron laser (XFEL) provides x-ray self-amplified spontaneous emission (SASE) FEL radiation in the wavelength range from 0.1 to 3 nm using three undulator systems. The SASE mode of operation at the European XFEL defines specific behavior of longitudinal and transverse coherence properties. In this paper, we describe the evolution of the temporal and transverse correlation functions along the undulator length, and we extract the corresponding evolution of coherence time and degree of transverse coherence as typical figures of merit. Generation of coherent radiation inside the FEL undulators is followed by beam transport to the experiments. During transport, the total number of coherent modes is preserved, but the wavefront can be disturbed, and we analyze the conditions under which this occurs. It is emphasized that the development of experimental observables for the degree of coherence and wavefront properties will be important for experiments using coherent x-ray radiation.

[3] Author to whom any correspondence should be addressed.

Contents

1. Introduction

Coherence of x-ray radiation attracted a lot of interest during the past years and many new applications in various areas of natural science were proposed and introduced [1]. Prominent examples are the development of imaging methods with higher spatial resolution and contrast sensitivity, and of photon correlation spectroscopy methods, enabling the measurement of the dynamical properties of soft-matter and amorphous materials. The experiments carried out at third generation synchrotron sources have been made possible by their low-emittance electron beams, leading to partial coherence of undulator radiation. However, due to the limited degree of coherence, x-ray experiments using synchrotron radiation are facing a number of limitations. The effects of partial coherence on x-ray scattering are discussed, e.g., in [2]. X-ray free-electron lasers (XFEL) provide, instead, nearly diffraction-limited x-ray sources. The resulting high degree of coherence of XFEL radiation enables the development of new experimental techniques, allowing for new scientific applications. Most prominent are proposals for imaging single particles [3] and nanomaterials [4] and for the investigation of dynamics using correlation spectroscopy [5].

Experiments using coherent x-ray radiation are sensitive to the transverse and longitudinal coherence properties and, in several cases, also to the properties of the radiation wavefront. The requirements with respect to these parameters have to be evaluated for each application and cannot be discussed in detail in this paper. Instead, we describe the coherence and wavefront properties of XFEL radiation using the case of sources and an exemplary x-ray beam transport of the European XFEL facility [6]. We describe the FEL process leading to coherent emission of x-ray radiation, which is a new quality compared to conventional synchrotron radiation emission. For FEL experiments, the qualitative and quantitative description of coherent FEL radiation will be an important aspect. However, experimental observables and techniques to determine these observables in fluctuating x-ray FEL experiments are a new field in instrumentation with only very few studies done so far (see for example [7, 8]). Also, recent developments using synchrotron radiation bear promising potential for application at XFELs [9].

The paper is organized as follows: in section 2, we introduce the FEL process and describe its consequences for the design and layout considerations of the European XFEL. We introduce some basic considerations for coherent x-ray radiation and a general description of the coherence properties of FEL radiation. Sections 3 and 4 focus on the temporal and

Table 1. Overview of photon beamlines, FEL undulators and scientific instruments. The photon wavelength ranges of FEL undulators and instruments are indicated.

Source	Wavelength	Instrument	Technique
SASE 1	0.1 nm	SPB	Coherent diffraction imaging by single particles
		MID	Coherent diffraction imaging by nanostructures
			X-ray photon correlation spectroscopy
SASE 2	0.1–0.4 nm	FXE	Time-resolved diffraction and scattering
			Time-resolved spectroscopy
		HED	X-ray generation of extreme states of matter
			X-ray probing of extreme states of matter
SASE 3	0.4–3.0 nm	SQS	Electron and ion spectroscopy
		SCS	Coherent diffraction imaging
			X-ray photon correlation spectroscopy
			Photon-in photon-out spectroscopy

spatial coherence properties of the European XFEL before introducing a figure of merit for coherent x-ray radiation in section 5. The wavefront properties of FEL radiation and the effects of propagation are considered in the following section before concluding.

2. The European x-ray free-electron laser (XFEL)

The European XFEL is conceived as a user facility for scientific application of FEL radiation in the soft to hard x-ray regime. Its radiation properties will enable experiments using time resolution in the few femtosecond regime, high-intensity radiation exceeding gigawatt peak power and fully coherent radiation. The proposed scientific applications of this user facility span a wide range from quantum optics to complex biological processes [6, 10]. An important property of the European XFEL is the possibility to conduct a much larger number of experiments per year than exploratory facilities like FLASH [11, 12], SCSS [13] or LCLS [14, 15] can achieve. For this purpose, the high-repetition-rate electron beam is distributed to two electron beamlines and, in the start-up scenario, three FEL undulators. One of the electron beamlines includes the undulators[4] SASE 1 and SASE 3 and the second beamline includes the undulator SASE 2. The three undulators serve six instruments, specialized for certain x-ray techniques and operating quasi-simultaneously. Additionally two undulators and four instruments will be added later. Table 1 gives an overview of the initial sources and instruments.

The European XFEL will provide FEL radiation in the entire range from 0.1 to 3.0 nm. Whereas the region from 0.1 to 1.6 nm can be reached for an electron energy of $\mathcal{E} = 17.5$ GeV, for softer x-ray radiation the electron energy needs to be somewhat lowered. For stable and continuous operation of the facility the electron accelerator operates only for a minimum of settings, and tunability of the photon energy is enabled by changing the undulator gap. Providing a sufficiently small electron beam emittance, photon wavelengths below 0.1 nm will become accessible by opening the gap of undulators SASE 1 and SASE 2. The XFEL beam parameters

[4] SASE: self-amplified spontaneous emission.

Table 2. Current undulator parameters and photon beam properties at the European XFEL for 17.5 GeV electron energy operation, after recent update [6].

	Units	SASE 1	SASE 2	SASE 3
Undulator period	mm	35.6	47.9	68
Undulator magnetic field	T	1	0.6–1.3	0.9–1.7
Undulator gap	mm	10	19–10	20–10
Wavelength range	nm	0.1	0.1–0.4	0.4–1.6
Source size (full-width at half-maximum, FWHM)	μm	70	85–55	60–70
Divergence (FWHM)	μrad	1	0.84–3.4	3.4–11.4
Bandwidth (FWHM)	%	0.08	0.08–0.18	0.2–0.3
Coherence time	fs	0.2	0.22–0.38	0.34–0.88
Pulse duration (FWHM)	fs	100	100	100
Photons per pulse	#	10^{12}	$1–16 \times 10^{12}$	$1.2–13 \times 10^{13}$
Peak brilliance	B	5×10^{33}	$5–2.2 \times 10^{33}$	$15–5 \times 10^{32}$

in table 2 have been simulated using an electron beam with rms normalized projected emittance $\epsilon_n = 1.4\,\mu$m corresponding to a geometrical emittance $\epsilon = \epsilon_n/\gamma \approx 0.04$ nm, bunch charge of 1 nC, peak current $I = 5$ kA, Gaussian temporal distribution width 80 fs (rms) and an energy spread $\sigma_E = 1.5$ MeV (rms). In the case of SASE 3, which uses the spent electron beam of SASE 1, an increased uncorrelated energy spread of 8 MeV is used, originating in the FEL process and acting back on the electron beam. The parameters given in table 2 have been simulated for an FEL operating in the SASE mode. Since the SASE process is intimately linked to the coherence properties of the emitted radiation, in the following we briefly review the SASE mechanism.

In general, an FEL consists of a relativistic electron beam and a radiation field interacting with each other while the electrons propagate through an undulator [16, 17]. In the SASE case, shot-noise fluctuations of the electron beam current density serve as an input signal to the FEL. These fluctuations in number of electrons originate from the random Poisson process of photo-emission in the photo-injector, which can be approximated with a Gaussian process. The random temporal and spatial fluctuations in the beam current density correspond to a modulation of the beam current density at all temporal and spatial frequencies simultaneously. When the electron beam enters the undulator, the process of radiation is initiated by the presence of the modulation at temporal frequencies close to the resonance frequency of the undulator $\lambda \simeq \lambda_w(1 + K^2)/(2\gamma^2)$. Here λ_w is the undulator period, $K = eH_w\lambda_w/2\pi m_e c^2$ is the undulator parameter, H_w is the rms value of the undulator field, $\gamma = \mathcal{E}/(m_e c^2)$ is the relativistic factor and $(-e)$ and m_e are the charge and the rest mass of the electron, respectively, with c being the velocity of light in vacuum. In the following, we will be using the CGS system.

In contrast to spontaneous radiation sources in an FEL, the interaction between electrons and radiation field is not negligible. The fields produced by the moving charges in one part of the undulator act back on moving charges in another part of the undulator resulting in a collective instability of the electron bunch, known as the FEL instability. This instability produces an exponential growth (along the electron propagation direction) of the modulation of the electron density around the resonance wavelength λ. At the same time, transversely, not all spatial frequencies are amplified in the same way. Thus, an FEL can be seen as an active

filter both for temporal and spatial frequencies. In contrast to passive filters, the filtering process takes place through a high-gain amplification process. As the beam travels through the high-gain FEL amplifier one can identify a linear regime, characterized by the exponential growth of the radiation power along the undulator, and a nonlinear regime, ending in saturation. In practice, an intensity gain in excess of 10^7–10^8 may be obtained in the x-ray range. The radiation power ceases to increase exponentially when the electron bunch is completely modulated according to shot noise at the resonant wavelength, and all electrons radiate almost in phase.

Let us now briefly discuss similarities and differences between coherence properties of radiation from modern third generation synchrotron radiation sources [1, 18, 19] at a typical wavelength of $\lambda = 0.1$ nm and SASE XFELs [20]. Due to the very small emittance, especially in the vertical plane, modern synchrotron radiation sources are characterized by a higher degree of transverse coherence compared to previous generations. Moreover, coherence properties are usually improved by spatial filtering with pinholes near the experiment and by means of monochromators, selecting a smaller bandwidth and therefore increasing the longitudinal coherence length. Both methods increase the coherence degree but substantially reduce the photon flux.

In contrast, at SASE FELs, the input shot-noise signal is, at the same time, amplified and filtered both in the temporal and in the spatial frequency domains. Thus spatial filtering is already included in the amplification process, providing a high degree of transverse coherence. However, while the longitudinal coherence in the hard x-ray regime is significantly improved with respect to non-monochromatized synchrotron radiation, it is still far from being complete.

Moreover, in the linear regime, FEL and synchrotron radiation sources share the same photon statistics. The filtering process is linear and, since the shot noise in the electron beam can be considered as a Gaussian random process, it follows that also the radiation constitutes a Gaussian random process. Both in the case of conventional synchrotron radiation and in the linear regime of a SASE FEL, the probability distribution of the instantaneous radiation intensity is a negative exponential. Furthermore, the integrals of the instantaneous intensity (instantaneous power, energy in the radiation pulse) and the integrated spectral density fluctuate in accordance with the gamma distribution [21, 22]:

$$p(W) = \frac{M^M}{\Gamma(M)} \left(\frac{W}{\langle W \rangle}\right)^{M-1} \frac{1}{\langle W \rangle} \exp\left(-M \frac{W}{\langle W \rangle}\right), \tag{1}$$

where $\Gamma(M)$ is the gamma function, $M = 1/\sigma_{\mathrm{W}}^2$ and $\sigma_{\mathrm{W}} = \sqrt{\langle (W - \langle W \rangle)^2 \rangle}$. In the case when W is the total energy in the radiation pulse, the parameter M can be interpreted as the average number of 'degrees of freedom' or 'modes'. Note that for the case of spontaneous synchrotron radiation sources with diffraction-limited vertical emittance, the horizontal emittance is still much larger than the radiation wavelength, meaning that M is determined by both longitudinal and transverse modes. For the SASE FEL case instead, M is usually dominated by longitudinal modes (e.g. a few hundreds for 0.1 nm radiation and a pulse duration of 100 fs) since the high degree of transverse coherence corresponds to a number of transverse modes near unity. Fluctuations reach their maximum value towards the end of the linear regime. When approaching the saturation point, statistical properties of the radiation change drastically on a scale of one field gain length [20]–[23]. The FEL now provides nonlinear filtering, and the statistics becomes non-Gaussian. One useful property of the nonlinear regime is a significant reduction in fluctuations of the radiation energy (down to a few per cent in the case of SASE 1 at 0.1 nm). The sensitivity of the radiation pulse energy with respect to fluctuating machine parameters also reduces significantly.

In the next two sections, we analyze the longitudinal and transverse coherence properties of the European XFEL. Statistical optics presents the theoretical tool for studying these properties in terms of correlation functions of the field [21, 24, 26]. In particular, temporal correlation functions describe longitudinal coherence of the radiation, whereas spatial correlation functions describe transverse coherence. We will limit ourselves to the study of first-order correlations.

3. Longitudinal coherence properties

In the longitudinal direction, the amplification bandwidth of the high-gain FEL amplifier is restricted by the resonance properties of the undulator. This bandwidth is determined by the number of undulator periods N_w within one gain length, the characteristic length of the exponential amplification process. Since we study the start-up from shot noise, we assume that the input current has a homogeneous spectral distribution. The FWHM spectrum of radiation is concentrated within a narrow band, $\Delta\lambda/\lambda \simeq (2\pi N_w)^{-1}$, corresponding to a typical amplification bandwidth of the order of 0.1% at a wavelength of 0.1 nm. At the same time the radiation pulse has a duration σ_T determined essentially by the electron bunch duration (compare table 2) and the single-shot power spectrum must contain Fourier-limited spikes of typical bandwidth $1/\sigma_T$. As a result, the spectral distribution contains hundreds of spikes, corresponding to poor longitudinal coherence. This can be seen in figure 1, which presents temporal and spectral distributions of single-pulse FEL radiation for the case of 0.1 nm radiation at the SASE 1 beamline.

Once the electric field $E(\vec{r}_\perp, z, t) = E_x + iE_y$ is known, the slowly varying amplitude $\widetilde{E}$ can be calculated from

$$E = \widetilde{E}(\vec{r}_\perp, z, t)\exp[i\omega_0(z/c - t)] + \text{c.c.}, \tag{2}$$

where ω_0 is the frequency of the fundamental. In the following we will only be dealing with the slowly varying amplitude of the field, and we will omit the '~' sign everywhere for simplicity. Then, the first-order temporal normalized correlation function can be written as

$$g_1(\vec{r}, t - t') = \frac{\langle E(\vec{r}, t)E^*(\vec{r}, t')\rangle}{\left[\langle|E(\vec{r}, t)|^2\rangle\langle|E(\vec{r}, t')|^2\rangle\right]^{1/2}}, \tag{3}$$

where brackets indicate an average over an ensemble of pulses. In this paper, we will consider the radiation process quasi-stationary, meaning that the averaged intensity of the radiation pulse is a slowly varying function of time with respect to the width of the correlation function g_1. This assumption is a good approximation in our case, as can be seen by inspection of figure 1. Then, the Wiener–Khintchine theorem holds, meaning that the spectrum $\langle|\bar{E}(\omega)|^2\rangle$, where $\bar{E}$ indicates the temporal Fourier transform of the electric field, and the temporal correlation function $\langle E(t)E^*(t')\rangle$ form a Fourier pair. This implies that also $\langle|\bar{E}(\Delta\omega)|^2\rangle$ with $\Delta\omega = \omega - \omega_0$ and $\langle E(t)E^*(t')\rangle$ form a Fourier pair. Simultaneously, the intensity $\langle|E(t)|^2\rangle$ and the spectral correlation function $\langle\bar{E}(\omega)\bar{E}^*(\omega')\rangle$ are also a Fourier pair. These properties can be verified from the analysis of the data in figure 1. It follows that the width of the temporal correlation function is related to the inverse of the spectral bandwidth, whereas the width of the spectral correlation function is related to the inverse temporal duration of the pulse.

In the stationary case, g_1 is a function of the difference $\tau = t - t'$ only. Following Mandel [24], the coherence time is subsequently defined in terms of g_1 as

$$\tau_c = \int_{-\infty}^{\infty} |g_1(\tau)|^2 d\tau. \tag{4}$$

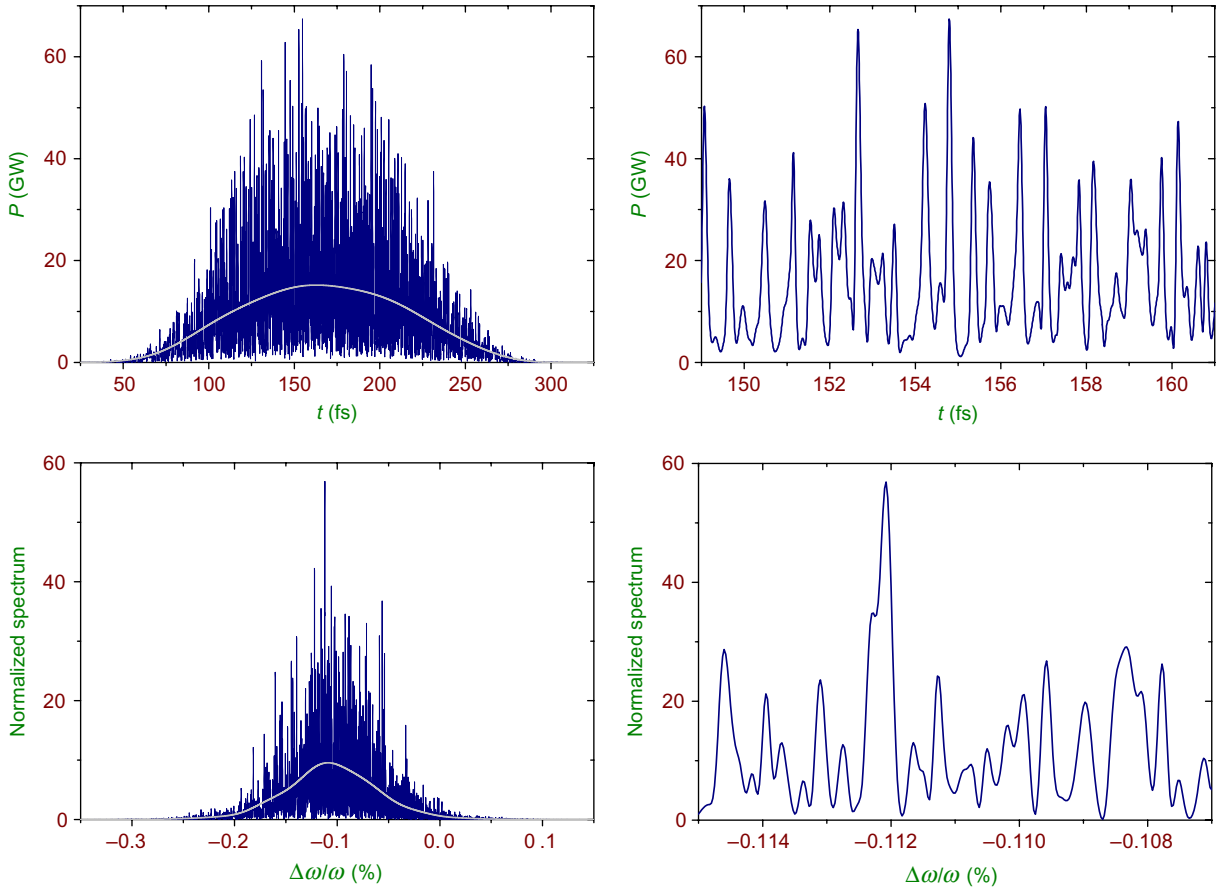

Figure 1. Temporal (top) and spectral (bottom) distributions of a single radiation pulse and a wavelength of 0.1 nm at SASE 1. Smooth lines show averaged profiles and the right side plots are enlargements.

The corresponding coherence times for the three SASE beamlines are indicated in table 2. The coherence time increases in the exponential gain regime, reaching a maximum near the saturation point, and then starts to decrease. This behavior is illustrated in figure 2 for different undulators of the European XFEL.

4. Transverse coherence properties

Transverse coherence properties can be studied in terms of the first-order transverse normalized correlation function:

$$\gamma_1(\vec{r}_\perp, \vec{r}'_\perp) = \frac{\langle E(\vec{r}_\perp) E^*(\vec{r}'_\perp)\rangle}{[\langle |E(\vec{r}_\perp)|^2\rangle \langle |E(\vec{r}'_\perp)|^2\rangle]^{1/2}}, \tag{5}$$

where the temporal dependence has been removed because of the quasi-stationary approximation. Equation (5) is the expression for the complex coherence factor given in [26], and is a function of two transverse positions. In figure 3, we present the modulus $|\gamma_1(\vec{r}_\perp, \vec{r}'_\perp)|$ of this function for SASE 1 for the special case when one of these positions is on-axis. In the same

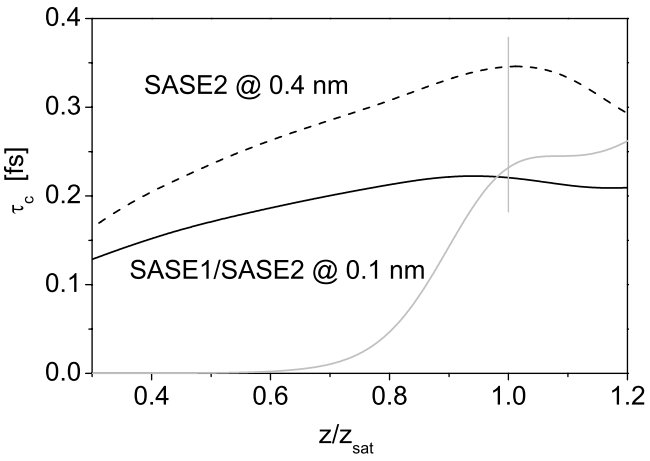

Figure 2. Evolution of the coherence time along the undulator. The solid curve corresponds to SASE 1 and SASE 2 operating at 0.1 nm. The dashed curve corresponds to SASE 2 operating at 0.4 nm. The gray curve indicates the evolution of the radiation power in SASE 1 operating at 0.1 nm wavelength. The propagation coordinate is normalized to the saturation length. Calculations have been performed with simulation code FAST [25].

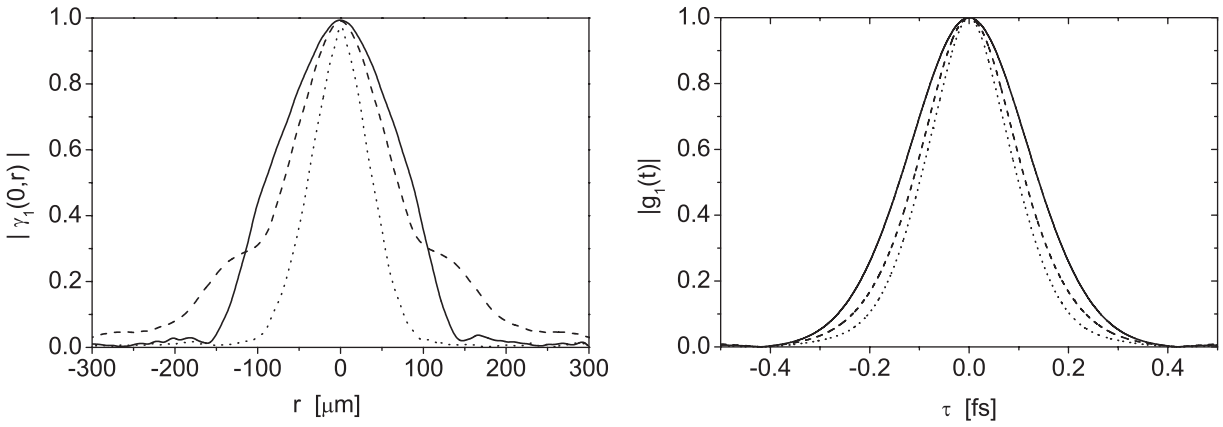

Figure 3. Moduli $|\gamma_1(r, 0)|$ of the first-order transverse correlation function and $|g_1(\tau)|$ of the first-order time correlation function for SASE 1 operating at the wavelength of 0.1 nm. Solid, dotted and dashed curves correspond to the saturation ($z = z_{\rm sat}$), linear regime ($z = 0.5z_{\rm sat}$), and deep nonlinear regime ($z = 1.5z_{\rm sat}$). Calculations have been performed with the simulation code FAST [25].

figure, the modulus of the temporal correlation function is presented. For the nonlinear regime we observe non-Gaussian behavior of $|\gamma_1(r, 0)|$.

The transverse coherence length is defined similar to equation (4) for the modulus of the first-order transverse normalized correlation function [24]

$$\xi_{\rm t}(\vec{r}_\perp) = \int_{-\infty}^{\infty} |\gamma_1(\vec{r}_\perp, \Delta r_\perp)|^2 {\rm d}\Delta r_\perp. \tag{6}$$

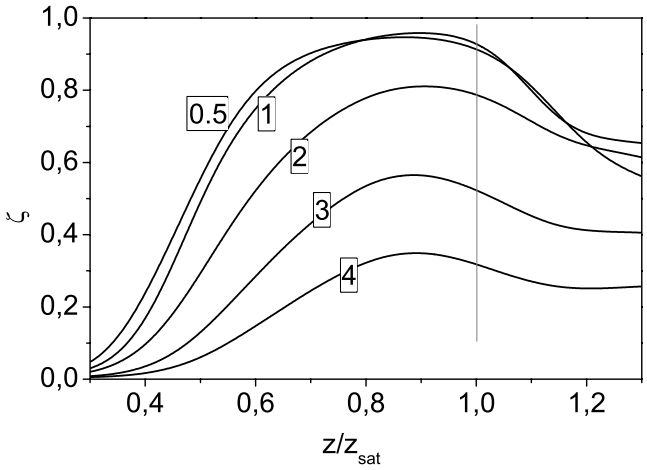

Figure 4. Evolution of the degree of transverse coherence along the undulator length for $\hat{\epsilon} = 0.5$, 1, 2, 3 and 4. The propagation coordinate is normalized to saturation length. Calculations have been performed with simulation code FAST [25].

In contrast to the coherence time, the transverse coherence length is a function of the transverse position $\vec{r}_\perp$. It is possible using further normalization in the transverse plane to define a single number for the transverse coherence, i.e. the degree of transverse coherence [27]:

$$\zeta = \frac{\int\int |\gamma_1(\vec{r}_\perp, \vec{r}'_\perp)|^2 \langle I(\vec{r}_\perp)\rangle \langle I(\vec{r}'_\perp)\rangle \mathrm{d}\vec{r}_\perp \mathrm{d}\vec{r}'_\perp}{\left[\int \langle I(\vec{r}_\perp)\rangle \mathrm{d}\vec{r}_\perp\right]^2}. \tag{7}$$

Above we have described that the formation of transverse coherence in SASE FELs happens due to transverse modes selection. It is convenient to use for the description the parameter $\hat{\epsilon} = 2\pi\epsilon/\lambda$. In the case of $\hat{\epsilon} < 1$ and optimization for highest growth rate of the FEL, the fundamental FEL eigenmode TEM_{00} amplifies much faster than high-order modes so that the latter are suppressed at the end of the linear regime before reaching saturation [28]. In the nonlinear regime, high-order modes start to grow again. Likewise, the highest degree of transverse coherence is obtained at this location. Figure 4 presents the degree of transverse coherence ζ versus the reduced propagation coordinate z/z_{sat} for different values of the parameter $\hat{\epsilon}$. Using $\hat{\epsilon}$ one obtains an estimate for the degree of transverse coherence at saturation for different wavelengths and undulators at the European XFEL. For instance, for SASE 1 at 0.1 nm, the conservative design value of the normalized emittance $\epsilon_{\mathrm{n}} = \gamma\epsilon = 1.4\,\mu$m [6], one finds $\hat{\epsilon} = 2.6$ corresponding to a degree of transverse coherence of about 65% at saturation. This value increases to about 90% for SASE 2 at 0.2 nm. An important observation is that the degree of transverse coherence in this quasi-stationary approximation depends strongly on the electron beam emittance. First results for hard XFELs indicate that values $\epsilon_{\mathrm{n}} \leqslant 0.5\,\mu$m can be achieved. For $\lambda = 0.1$ nm, $\hat{\epsilon}$ then becomes smaller than unity and a degree of transverse coherence of the order of 95% can be expected. It follows that experiments requiring a high degree of transverse coherence are in need of operating the electron beam with minimized emittance.

Simulations using the code FAST [25] shown in figure 5 further indicate that the divergence of FEL radiation in the far field ($\lambda L/(2\pi\sigma^2) \gg 1$ for a distance L to the source of size σ) can decrease considerably when going from the linear regime via saturation to the deep nonlinear regime.

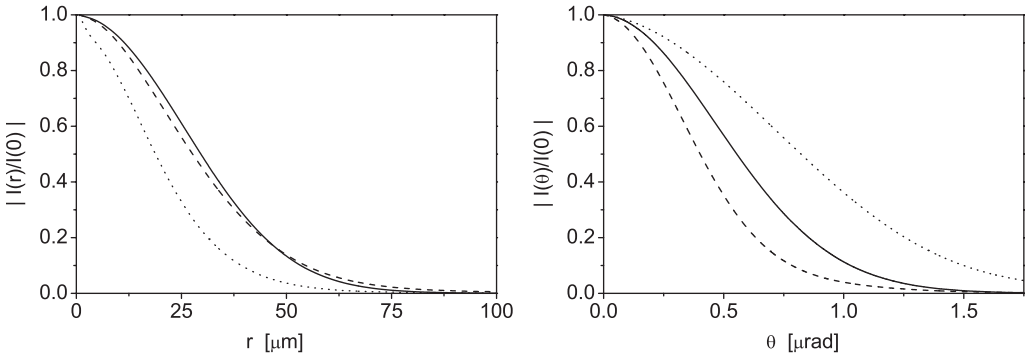

Figure 5. Intensity distribution of the radiation in the near and far fields for SASE 1 operating at 0.1 nm (left and right plots, respectively). Solid, dotted and dashed curves correspond to the saturation ($z = z_{\mathrm{sat}}$), linear regime ($z = 0.5z_{\mathrm{sat}}$) and deep nonlinear regime ($z = 1.5z_{\mathrm{sat}}$).

5. Degeneracy parameter

In order to characterize x-ray sources, two figures of merit for the FEL coherence properties are of importance, the peak brilliance and the degeneracy parameter. The peak brilliance B_r is naturally related to the degree of transverse coherence by [27]

$$B_r = \frac{\omega \mathrm{d}\dot{N}_{\mathrm{ph}}}{\mathrm{d}\omega} \frac{\zeta}{(\lambda/2)^2} \tag{8}$$

with $\dot{N}_{\mathrm{ph}}$ being the photon flux. B_r is further related to the second figure of merit. The degeneracy parameter δ corresponds to the number of photons per coherent mode (longitudinal and transverse). In the case of our quasi-stationary model it is given by

$$\delta = \dot{N}_{\mathrm{ph}} \tau_{\mathrm{c}} \zeta. \tag{9}$$

Assuming a Gaussian shape for the spectrum of the SASE FEL radiation (which is true in the high-gain linear regime, and is approximately true at saturation as well) one can show that [27]

$$B_r = \frac{4\sqrt{2}c}{\lambda^3}\delta. \tag{10}$$

Due to high gain of the amplification process and the exceptionally bright electron beams, the peak brilliance and the degeneracy parameter of XFELs are many orders of magnitude higher than those of third generation light sources [10]. In particular, for SASE FELs operating at 0.1 nm the peak brilliance is in the range of 10^{33}–10^{34} photons $\mathrm{s}^{-1}/0.1\%\mathrm{BW}\,\mathrm{mm}^{-2}\,\mathrm{mrad}^{-2}$, and the degeneracy parameter is of the order of 10^9. As is well known, the degeneracy parameter can be seen from a quantum viewpoint as the expected number of photons in the same quantum state [24]. Its value is critical, e.g. when trying to distinguish statistical properties of radiation by means of photocount procedures [26].

6. Wavefront propagation

Coherence experiments typically exploit interferences of radiation scattered by the sample. Although these experiments in general require coherence in transverse and longitudinal

Table 3. Parameters for wavefront propagation analysis.

	Unit	SASE 1	SASE 2	SASE 3
Wavelength	nm	0.1	0.1/0.4	0.4/0.8/1.6
Photon beam divergence (FWHM)	μrad	1	0.84/3.4	3.4/6.8/11.4
Approximate distance from undulator exit to the source[6]	m	-55	$-80/-5$	-10
Distance z_1 (undulator to M1)	m	525	525	234
Distance z_2 (M1 to end station)	m	430	430	166
Incidence angle	mrad	1.8	1.8	10
$4\sigma_{\mathrm{rms}}$ beam footprint at M1	mm	500	480/1700	140/250/420
rms surface height errors (Marechal criterion)	nm	2	2/8	1.4/2.8/5.5
Relevant spatial range	mm	0.5 . . . 180	0.5 . . . 180/340	0.1 . . . 20/30/40

properties, we are considering in this section only transverse coherence properties. The experimental observable, the interference pattern, depends furthermore on the wavefront properties of the radiation. While the coherence properties are typically determined only by the source and do not change during the transport of the x-ray beam[5], the wavefront properties depend significantly on the x-ray beam transport. It is therefore of importance to study the impact of propagation through the XFEL optical system on the quality of radiation wavefronts delivered to the experiment. Such an impact is obviously relevant also for the achievement of a tight photon beam focus required for many experiments.

As an example, we use the classical Young experiment, where the interference of radiation originating from two pinholes at positions $\vec{r}_\perp$ and $\vec{r}'_\perp$ is registered in the observation plane. The fringe visibility V of the interference pattern varies according to

$$V(\vec{r}_\perp, \vec{r}'_\perp) = 2\frac{\langle I(\vec{r}_\perp)\rangle^{1/2}\langle I(\vec{r}'_\perp)\rangle^{1/2}}{\langle I(\vec{r}_\perp)\rangle + \langle I(\vec{r}'_\perp)\rangle}|\gamma_1(\vec{r}_\perp, \vec{r}'_\perp)|. \tag{11}$$

The visibility V depends both on the modulus of the transverse correlation function and on how the averaged field intensity varies between $\vec{r}_\perp$ and $\vec{r}'_\perp$. Therefore, the visibility can degrade while the degree of transverse coherent radiation is not affected. Similarly, the position of the interference fringes in the observation plane is influenced by the phase difference of the electric fields at $\vec{r}_\perp$ and $\vec{r}'_\perp$. Hence, when an experiment is planned, not only should the transverse coherence length ξ_t be larger than the sample size but also the field should be nearly constant in amplitude and phase over the sample dimension.

The passage of radiation through optical elements is described in terms of wavefront propagation, i.e. in the framework of wave optics. For grazing incidence optics, mirrors are coherently illuminated and we can use a completely deterministic description. In the following, we show the effects of a single grazing incidence mirror on the propagation of coherent radiation for the cases of the SASE 1 and SASE 3 beam transport systems of the European XFEL [6]. The small divergence and bandwidth and the high degree of transverse coherence of XFEL radiation allow us to use scalar diffraction theory in paraxial approximation [29]. Despite the large distance $L \simeq 500\,\mathrm{m}$ (compare table 3) of the optical elements to the observation plane

[5] Here we do not consider mixing of transverse and longitudinal modes that diffraction on a monochromator can cause.

[6] Estimated using ZEMAX code and beam sizes and far-field angular divergences extracted from table 2.

and due to the short wavelength $\lambda = 0.1$ nm, the characteristic size of imperfections of the mirror a does not satisfy the far field condition, $\lambda L/(2\pi a^2) \gg 1$. Therefore, the treatment of wavefront propagation must rely on Fresnel rather than Fraunhofer diffraction theory. To further account for diffraction effects accompanying the coherent beam reflection at long grazing incidence mirrors, one cannot profit from Fourier optics. For our analysis we use a stationary phase approximation implemented in the code PHASE [30] and numerical calculations of the Fresnel–Kirchhoff integral.

Wavefront properties are in particular affected by an imperfect shape function of the optical elements, including slope errors, medium range distortions of surfaces, waviness and short-range surface roughness, and by the effective aperture of these optics. Mirrors to be employed at the European XFEL require extremely smooth surfaces. Their quality is described by the one-dimensional power spectrum density (PSD)

$$S(f) = \frac{1}{L}\left|\int_{-1/2L}^{1/2L} \mathrm{d}x\; h(x)\exp(2\pi \mathrm{i} f x)\right|^2. \tag{12}$$

Here $h(x)$ are the height deviations of the real surface shape from the ideal one and x is the variable along the optical surface. For the wavefront phase distortions $\Delta\Phi(x) = 2\pi\Delta w(x)/\lambda$, we find $\Delta w(x) = 2\,h(x)\sin\theta$ for the incidence angle θ. In coherent optics the rms Marechal criterion $\Delta w_{\mathrm{rms}} < \lambda/14$ was introduced as a condition for acceptable aberrations [31].

In the analysis of all distortion types, those on the length scale of the beam footprint turn out to be most critical. These imperfections lead to a distortion of the reflected beam wavefront, creating a one-dimensional speckle pattern in the observation plane at distances of hundreds of meters [32]. Speckle contrast and characteristic sizes depend on the size of the x-ray beam impinging on the mirror and on distances between source, mirror and the observation plane. The wavefront distortions on the scale of radiation wavelength are most important for the formation of these speckles, thereby providing a hint of the most critical deviations h. These deviations correspond to the medium frequency components of the PSD. In table 3, the height error h satisfying the Marechal criterion is indicated for several wavelength and incidence angles.

The range of the relevant spatial frequencies can be roughly estimated from the width of Fresnel zones projections on the mirror surface $\Delta r_n/\sin\theta$. The width of the Fresnel zone is $\Delta r_n \cong (\sqrt{n} - \sqrt{n-1})\sqrt{\lambda L_{\mathrm{eff}}}$ for the Fresnel zone number n, $1/L_{\mathrm{eff}} = (1/z_1 + 1/z_2)$, and z_1 and z_2 are the source-to-mirror and mirror-to-observation plane distances. The shortest component corresponds to the width of the outermost zone projection for a given beam size. Characteristic lengths of the medium surface PSD components are shown in table 3. To minimize diffraction effects during reflection of the transverse coherent beam, the mirror length must be adequate to accept a significant part of the beam profile. It is found that for an effective aperture larger or equal to $4\sigma_{\mathrm{rms}}$ the effects of diffraction by the mirror edges are reduced to the level of distortions caused by other technologically relevant mirror imperfections.

To demonstrate how the mirror imperfections change the properties of the coherent x-ray beam, we consider illumination of a plane mirror by monochromatic Gaussian beams with wavelength of 0.1 and 1.6 nm. Other properties are given in table 3. The calculations were carried out for a set of medium spatial frequency data, derived from the measured surface profile of a 510 mm long plane mirror installed at an FEL beamline at FLASH/DESY [33] (see figure 6). The original profile A proved to be unacceptable for hard XFEL radiation. For the cases of the optimized and parameterized profiles B and C, numerical solutions of the two-dimensional Kirchhoff integral were carried out [34]. The profile B, optimized for long-range

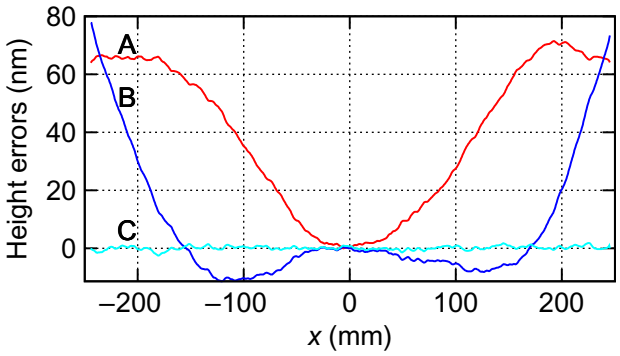

Figure 6. The red curve A is the height profile of a plane mirror used at FLASH [33]. Dark blue curve B has been derived from A by subtracting a 200 km curvature radius arc. For the light blue curve C in addition a spline curve with 23 mm step size has been applied.

bending, appeared to be sufficiently good for handling a coherent beam with $\lambda = 1.6$ nm. The profile C with additional spline correction corresponding to an idealized bimorph mirror [35] satisfies the most severe requirements imposed by 0.1 nm FEL radiation. The reflected beams (figures 7(a) and 7(c)) are smooth, compact and satisfy well the design beam parameters at the user stations. Nevertheless beam profile effects due to diffraction by the effective aperture and due to surface imperfections are observable in both cases.

As many experiments at the European XFEL [6] require focusing of the x-ray beam to sub-μm spots, we have also modeled focusing of the beam after reflection by mirror surfaces B and C using a perfect ellipsoidal mirror. The calculations were done using PHASE code for the stationary phase approximation [30]. The results are shown in figures 7(b) and 7(d). For both given profiles, one obtains a moderate blurring of the focus in the tangential direction, and the spot itself is well confined and appears to have well-defined smooth edges. The focal spot FWHM diameters correspond to 200 nm and 1 μm for the SASE 1 and SASE 3 cases, respectively. The focal spot size at 1.6 nm is still far from the value 0.35 μm defined by demagnification factor 2 : 400, due to the insufficient quality of the mirror with profile B.

7. Conclusions

We have presented an analysis of the coherence and wavefront properties of x-ray FEL radiation using the exemplary case of the European XFEL. In contrast to incoherent synchrotron radiation, the SASE FEL process corresponds to active filtering of the amplified shot-noise radiation, thereby providing high transverse and limited longitudinal coherence of the radiation by the source without further means. Correspondingly the single parameter degree of coherence ζ is much larger for FEL than it is for synchrotron radiation. As a figure of merit the peak brilliance and the degeneracy parameter can be applied to characterize highly coherent x-ray radiation.

Analyzing the degree of coherence in terms of the electron beam parameters we find that the ratio $\epsilon_n/\mathcal{E}$ of the normalized emittance over the electron energy provides good scaling. With current performance of high-energy electron accelerators, coherence degrees of 95% can be enabled.

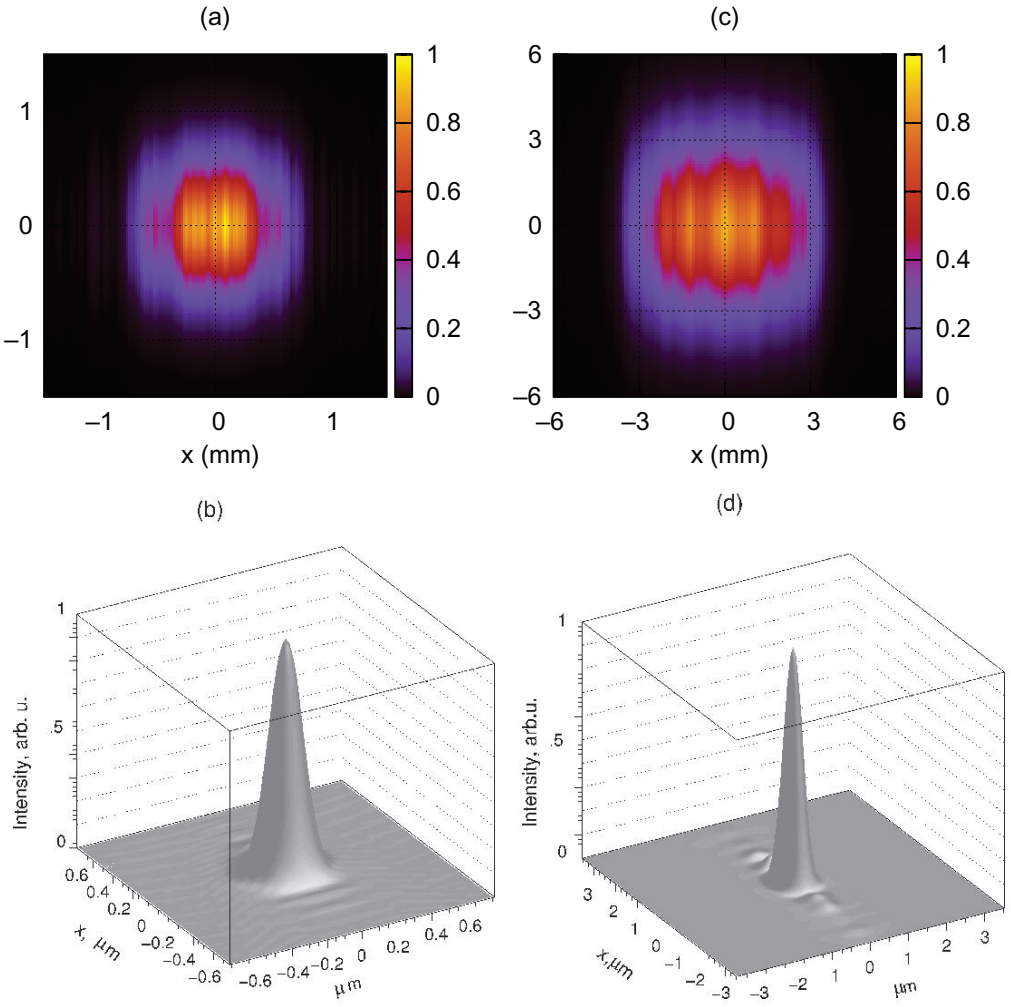

Figure 7. Reflected beam intensity distributions. On the left side, (a) is the unfocussed beam profile at distance 435 m from the mirror, and (b) is this beam focused by a perfect elliptical mirror with 2 m focal length for SASE 1, a wavelength of 0.1 nm and profile C. On the right, (c) is the unfocused beam profile at 234 m from the mirror, and (d) is this beam focused by a perfect elliptical mirror with 2 m focal length for SASE 3, a wavelength of 1.6 nm and profile B.

The coherence and wavefront properties are determined initially by the FEL source. In the transport of the radiation from the source to the experiment the optical elements do not affect the coherence, but the wavefront properties generally change. Since experiments are sensitive to the fringe visibility including both transverse coherence and wavefront properties, it is important to analyze the alteration of the wavefront and to estimate the consequences for the experiments due to this effect. We find that for hard x-ray radiation and the case of grazing incidence mirrors, very tight tolerances for the height error of the mirror follow. Since relatively long mirrors are needed and the tolerances cannot be matched by existing technology, it will be important to develop new methods of defining the mirror shape and to consider different ways of focusing.

References

[1] Lengeler B 2001 *Naturwissenschaften* **88** 249
[2] Sinha S, Tolan M and Gibeaud A 1998 *Phys. Rev.* B **57** 2740
[3] Neutze R *et al* 2000 *Nature* **406** 752
[4] Vartaniants I *et al* 2007 *J. Synchrotron Rad.* **14** 453
[5] Gruebel G *et al* 2007 *Nucl. Instrum. Methods* B **262** 357
[6] Altarelli M *et al* (ed) 2006 XFEL, the European x-ray free-electron laser *Technical Design Report DESY* 2006-097 Hamburg
[7] Ischebeck R *et al* 2003 *Nucl. Instrum. Methods Phys. Res.* A **507** 175
[8] Mitzner R *et al* 2008 *Opt. Express* **16** 19909
[9] Alaimo M D *et al* 2009 *Phys. Rev. Lett.* **103** 194805
[10] Richard F *et al* 2001 *Technical TESLA Design Report* DESY 2001-011 and http://tesla.desy.de/
[11] Ayvazyan V *et al* 2006 *Eur. Phys. J.* D **37** 297
[12] Ackermann W *et al* 2007 *Nat. Photonics* **336** 1
[13] Tanaka T and Shintake T (ed) 2005 *SCSS X-FEL Conceptual Design Report* (Hyogo, Japan: Riken Harima Institute) (see also http://www-xfel.spring8.or.jp)
[14] Arthur J *et al* 2002 Linac coherent light source (LCLS) *Conceptual Design Report* SLAC-R593, Stanford (see also http://www-ssrl.slac.stanford.edu/lcls/cdr)
[15] Emma P 2010 First lasing of the LCLS x-ray FEL at 1.5 Å *Proc. PAC09, Vancouver* to be published in http://accelconf.web.cern.ch/AccelConf/
[16] Pantell R H, Soncini Y and Putthoff H E 1968 *IEEE J. Quantum Electron.* **11** 905
[17] Madey J M J 1972 *J. Appl. Phys.* **43** 3014
[18] van der Veen J F and Pfeiffer F 2004 *J. Phys.: Condens. Matter* **16** 5003
[19] Geloni G, Saldin E, Schneidmiller E and Yurkov M 2008 *Nucl. Instrum. Methods Phys. Res.* A **588** 463
[20] Saldin E L, Schneidmiller E A and Yurkov M V 2010 *New J. Phys.* **12** 035010
[21] Saldin E L, Schneidmiller E A and Yurkov M V 1999 *The Physics of Free Electron Lasers* (Berlin: Springer)
[22] Saldin E L, Schneidmiller E A and Yurkov M V 1998 *Opt. Commun.* **148** 383
[23] Saldin E L, Schneidmiller E A and Yurkov M V 2003 *Nucl. Instrum. Methods* A **507** 106
[24] Mandel L and Wolf E 1995 *Optical Coherence and Quantum Optics* (Cambridge: Cambridge University Press)
[25] Saldin E L, Schneidmiller E A and Yurkov M V 1999 *Nucl. Instrum. Methods* A **429** 233
[26] Goodman J W 1985 *Statistical Optics* (New York: Wiley)
[27] Saldin E L, Schneidmiller E A and Yurkov M V 2008 *Opt. Commun.* **281** 1179
[28] Saldin E L, Schneidmiller E A and Yurkov M V 2000 *Opt. Commun.* **186** 185
[29] Goodman J W 1996 *Introduction to Fourier Optics* 2nd edn (New York: McGraw-Hill)
[30] Bahrdt J 2007 *Phys. Rev. Spec. Top. Accel. Beams* **10** 060701
[31] Born M and Wolf E 2003 *Principles of Optics* (Cambridge: Cambridge University Press)
[32] Yabashi M *et al* 2005 *J. Phys. D: Appl. Phys.* **38** A11
[33] Tiedke K *et al* 2009 *New J. Phys.* **11** 023029
[34] Bahrdt J private communications
[35] Signorato R, Hignette O and Goulon J 1998 *J. Synchrotron Rad.* **5** 797